

Why is Uranus so Cold?

Hannah J. Petrovic

Submitted: April 20, 2020

Level 4 Project, MPhysics and Astronomy

Supervisor: Dr V. Eke

Department of Physics, Durham University

Abstract

Despite the similarities between the ice-giants Uranus and Neptune, several key characteristics are known to be very different, including, but not limited to, the obliquity and energy balance. Here, plausible mechanisms to explain the low heat flux from Uranus in comparison to the other outer solar system planets are explored. There exist three leading hypotheses to resolve this: a period of accelerated cooling, a deviation in the planetary bond albedo derived from Voyager 2 data, and a potential giant impact into the planet. The focus here is on the giant impact hypothesis, presenting results of two 10^6 particle 3D SPH simulations using SWIFT, examining the influence of giant impacts of $2M_{\oplus}$ and $3M_{\oplus}$ impactors into initially non-rotating proto-Uranus targets. The masses follow from [Kegerreis et al. \(2018\)](#) who previously recreated key characteristics of the planet, such as its rotation rate and obliquity. An impact parameter of $b = 0.7$ is used for each impact. Notably, the viability of impactor core material to create a series of diffusive layers on the proto-Uranus core post-impact is investigated as this could reproduce the expected effect of inhibiting heat flux at the surface by effectively trapping heat in the core itself. Observing the distribution of the impactor's core material shows shell coverage at the Uranus core-mantle boundary of 78% and 67% for the $2M_{\oplus}$ and $3M_{\oplus}$ impactors respectively, using impactor core material within radial intervals 1σ from the mean position of the impactor's core in the planet. Removing any overlapping of these areas using map projections from the sphere to a 2D plane, the area coverage is reduced to 72% and 65%. The remaining coverage suggests a high proportion of the layer can be covered by this material regardless. Examining the distribution of the internal energies of particles at the end of the simulation also inform of the potential for a short period of accelerated cooling from high internal energy particles post impact and the potential for small cell layered convection and turbulent diffusion at the core-mantle boundary. Further work is needed to connect the distribution of particles to the resulting heat flux from the planet, and calculate expected cooling times given the impactor's material placement on the proto-Uranus.

Contents

1	Introduction	2
2	Method and Theory	4
2.1	Planetary Thermodynamics	4
2.1.1	Planetary Cooling	5
2.1.2	Equations of State (EoS)	6
2.1.3	Stability Criteria	7
2.1.4	Internal Fluid Structures	7
2.1.5	Clouds and Condensation	8
2.2	Simulation Methods	9
2.2.1	Smoothed Particle Hydrodynamics (SPH)	9
2.2.2	SWIFT	10
2.2.3	Planetary Profiles	10
2.2.4	Initial Conditions	11
2.3	Details of Simulation Runs	15
3	Results	16
3.1	Particle Distribution	16
3.1.1	Impactor Radial Placement	16
3.1.2	Impactor Core Coverage	19
3.2	Internal Energies	20
4	Discussion	23
4.1	Equations of State	24
4.2	Bond Albedo Uncertainty	24
4.3	Exoplanet Diversity	25
4.4	Advancing Simulations	26
5	Conclusion	27
	Acknowledgements	28
	References	28

1 Introduction

The Voyager space probes, launched in 1977, had the unique opportunity to garner a wealth of data from the outermost reaches of our solar system, with both now outside the heliosphere itself. This provided close up data and images of the giant planets and brought many mysteries to the forefront of astronomy. Due to the flight trajectories, only Voyager 2, launched prior to Voyager 1, had the chance to collect data from all four giants in our solar system, with Voyager 1 not conducting flybys of Uranus or Neptune.

Voyager 2 reached its closest approach to Uranus during January 1986. Images from this flyby showed the familiar blue haze of the planet, a consequence of Rayleigh scattering from

methane in the atmosphere. Measurements taken of the planet revealed an inconsistent result when compared with the other giants, that Uranus has a heat flux much lower than expected. This is often referred to as the 'energy balance' and describes the ratio of thermal flux from the planet to that provided by the star. For Uranus this value lies at 1.06 ± 0.08 (Pearl et al., 1990), whereas for Jupiter, Saturn and Neptune, these values are 1.67 ± 0.09 , 1.78 ± 0.09 , and 2.61 ± 0.28 (Hanel et al., 1981, 1983; Pearl & Conrath, 1991). Taking into consideration their respective solar distances, these measurements confirmed that Uranus is much cooler relative to the other giant planets, to the extent where it is presently almost in equilibrium with the solar insolation. With its close resemblance in many ways to Neptune, for example in mass, size, and therefore mean density, surface temperature, rotation rate, ice-to-rock ratio and so forth, this is a peculiar result. Further utilising gravitational moments determined for the planets by Voyager, cooling times computed assuming adiabatic interiors for the planets suggest that much longer timescales than the age of our solar system at 4.56 Gyrs are required to explain the low heat flux of Uranus, whereas similar models for Neptune correctly propose that the planet is still cooling (Fortney et al., 2011; Nettelmann et al., 2013). This discrepancy between the two planets must therefore be explained by an alternative scenario to these standard calculations.

With its notoriously high obliquity at 98° (Tremaine, 1991) and with its regular satellites corotating in this frame, while Neptune harbours an obliquity of only 27.7° , a frequent hypothesis to explain this difference is a giant impact into Uranus (Safronov, 1966; Stevenson, 1986). Reinhardt et al. (2019) and Kurosaki & Inutsuka (2018) show using hydrodynamic simulations that a collision of this nature can subsequently create sufficient material for a debris disc to form around the planet, with enough rocky material to later form Uranus' satellites. However, using initial conditions for these debris discs inferred from these hydrodynamic simulations, Ishizawa et al. (2019) show using direct N -body simulations that the distribution of these satellites cannot be explained using the surface density produced from a giant impact. Nevertheless, they do continue to state that this is a plausible method to create satellites orbiting in this way and further work is needed to consider the thermal and viscous evolution of such a disc for a more thorough analysis.

If a giant impact did occur in Uranus' history, connecting this to the temperature of the planet and investigating cooling times is essential. Podolak et al. (1991) suggested that a series of composition gradients may suffice to explain the present heat flux. These could create a mean molecular gradient leading to a set of diffusive interfaces within which convection can occur. With heat transport through diffusion leading to much longer cooling times than through convection processes, this would inhibit heat flux outwards from the planet, effectively trapping heat under these layers in the centre of the planet whilst ensuring a surface temperature lower than otherwise. Due to the similarities between Uranus and Neptune, a significant event, such as a giant impact, may be necessary to create the molecular gradients required.

A giant impact may well also be able to explain the offset magnetic field of the planet which is thought to be centred $\sim 0.33R_U$ from the centre of the planet within convective ionic oceans. This dipole is also tilted relative to the rotation axis by a further 59° . For Neptune, the centre offset is larger at $\sim 0.55R_N$ but with only a 47° tilt from the rotation axis (Nellis, 2015). Gómez-Pérez & Heimpel (2007) have shown that the planetary dynamo of both Uranus and

Neptune can be created from convective fluid flows within such an ionic layer using numerical simulations. Furthermore, [Stanley & Bloxham \(2004\)](#) suggest that the strange behaviour of these fields, relative to the other planets, can be described by an alternative geometry such as convection in thin shells. Models presented to explain the origin and cosmogony of Uranus and Neptune must be able to explain the offset magnetic field and tilt for both Uranus and Neptune. To date, the only magnetic field data currently available is that from Voyager, and since this only spans a short time interval of each flyby, it remains uncertain as to whether these fields vary throughout their seasons, and will remain so until further data can be taken.

An alternative to produce the low heat flux of Uranus resides in an accelerating cooling of the planet as suggested by [Kurosaki & Ikoma \(2017\)](#). They propose that the latent heat of condensation from volatiles such as H_2O , NH_3 , and CH_4 can keep the atmosphere hot. They show that this could lead to an accelerated cooling of Uranus, reproducing the present day heat flux as long as the planet is sufficiently polluted initially. They further suggest that a giant impact could potentially dredge up these materials from within the icy layer and upon re-accretion the atmosphere becomes highly polluted leading to this accelerated cooling of the planet.

Recent work by [Vazan & Helled \(2019\)](#) also suggest that thermal evolution with an interior consisting of an ice and rock mixture instead of differentiated shells is consistent with measurements. A mixture instead of differentiated homogeneous layers could be a consequence of a giant impact although this connection to cooling calculations has yet to be studied. Here, following from the first simulations of a giant impact into a proto-Uranus conducted by [Slattery et al. \(1992\)](#), and the advances made by [Kegerreis et al. \(2018\)](#) using high resolution simulations, we aim to address whether the giant impact scenario is a plausible mechanism to describe the heat flux we observe, creating an ice and rock mixture in the impact as used in [Vazan & Helled \(2019\)](#). The distribution of the particles and energies post-impact will be investigated. For this we utilise 3D smoothed particle hydrodynamic simulations and corresponding post-impact thermodynamic evolution models. In Section 2 the methods used to run these simulations and the physics involved are described, in Section 3 the results from the simulations ran are detailed and these are discussed further within Section 4. Concluding remarks are made in Section 5.

2 Method and Theory

In this section we describe relevant physics and the numerical methods used to investigate the subject area. We start with the fundamental thermodynamics, a consideration of how fluid motion can influence heat transfer within a giant planet, and detail the smoothed particle hydrodynamics technique along with the parameters used to create and simulate the giant impacts.

2.1 Planetary Thermodynamics

Accurate application of thermodynamics to derive cooling rates is necessary to investigate the long term heat flux in order to compare calculations with current observations. Planetary cooling is briefly described along with consideration of the composition of the planet under various

thermal and pressure circumstances with equations of state. Stability criteria for convection and other fluid structures are also outlined.

2.1.1 Planetary Cooling

Methods to understand the cooling rate of planetary interiors are derived from [Hubbard \(1973\)](#). In these one must consider the flux rates into and out of the planet. Incident flux on a planet is predominantly in the form of solar radiation, and the flux outwards is primarily due to the energy of accretion during formation. This occurs from the agglomeration of planetesimals onto the initial core in this formation model, where the material transfers its kinetic energy into thermal energy, heating the planet. Considering the accretion model of planetary formation and the ensuing high interior temperatures, standard calculations suggest it is surprising that Uranus is the only giant planet in our Solar System that exhibits a flux in equilibrium with the solar incident radiation.

The first thermal evolution models of Uranus and Neptune were conducted by [Hubbard \(1978\)](#). Since then, these models have been made more advanced, using planet specific parameters rather than scaled models as was the case of [Hubbard \(1978\)](#) from Jupiter cooling models in [Hubbard \(1977\)](#). More modern cooling models derived in [Fortney et al. \(2011\)](#) use radiative-convective model atmosphere grids to compute the cooling times of Uranus and Neptune.

Regardless of the method used, the albedo of the planet must be taken into account to calculate the flux that is absorbed by the planet. For Uranus this was determined from the measurements and images taken by Voyager 2 during its closest approach between January 15th and February 2nd 1986. In order to determine this value, measurements from broadband radiometric observations from the range of phase angles, also known as angles of reflectance, $15^\circ < \alpha < 155^\circ$, was used with extrapolations to compute the phase integral, q , from

$$q \equiv 2 \int_0^\pi \frac{I(\alpha)}{I(0)} \sin \alpha d\alpha \quad (1)$$

where α is the phase angle, described as the angle between the source of the radiation and the observing direction ([Pearl et al., 1990](#); [de Pater et al., 2002](#)).

Given the phase integral, the annual bolometric bond albedo, A , is determined using $A = pq$, where p is the geometric albedo determined by

$$p = \left(\frac{1329 \times 10^{-\frac{H}{5}}}{D} \right)^2. \quad (2)$$

Here, H is the absolute magnitude and D is the diameter in km ([Chesley et al., 2002](#)). For Uranus, the result is $A = 0.300 \pm 0.049$ ([Pearl et al., 1990](#)). This has frequently been used in cooling calculations of Uranus, however, in Section 4.2 we investigate whether this is a reliable measurement. This value can only be computed reliably from Earth for planets within 1AU where the full range of phase angles are accessible, but for the outer planets this value can only be calculated with data from spacecraft.

2.1.2 Equations of State (EoS)

To describe the planetary interior beyond simple models, it is necessary to include Equations of State (EoS) for the materials that compose the planet. These are used to describe the behaviour of the constituents under various pressure and temperature conditions. They can be incorporated into our simulations and for this we utilise the EoS for each layer of the planet: the rocky core, icy mantle and atmospheric envelope, from [Hubbard & Macfarlane \(1980, hereafter HM80\)](#). Zero temperature relations for the rocky core and icy mantle are used.

The core of Uranus is thought to be composed of 38% SiO₂, 25% MgO, 25% FeS and 12% FeO (HM80). The EoS describing this layer is derived from theoretical EoS from [Zharkov & Trubitsyn \(1978\)](#) alongside the additive volume law which allows the relative contributions of each material to be taken into account. For a mixture, Z, this would take the following form:

$$\frac{1}{\rho(p,T)} = \sum \frac{X_j}{\rho_j(p,T)}, \quad (3)$$

where the X_j are mass fractions of the various components of the mixture ([Vazan et al., 2015](#)). From this we can solve for $\rho(p,T)$ which describes the behaviour of this mixed material. The resulting EoS for the rocky core is,

$$P_0 = \rho^{14.563} \exp(-15.041 - 2.130\rho + 0.0483\rho^2), \quad (4)$$

where P_0 is the zero-temperature pressure in Mbar and ρ is in gcm⁻³.

The zero temperature equation for the icy mantle, from HM80, composed of 56.5% H₂O, 32.5% CH₄ and 11% NH₃ is then described using,

$$P_0 = \rho^{4.067} \exp(-3.097 - 0.228\rho - 0.0102\rho^2), \quad (5)$$

limited to use up to ~ 8 Mbar.

The atmosphere is mostly composed of a mixture of H₂ and He on Uranus. Due to the more complex nature of these constituents under the pressure and temperature variations, from a gaseous state into a coupled liquid state, the thermodynamic properties during this transition must be taken into account. Small amounts of other molecules, such as CH₄ at 2.3% ([Lindal et al., 1987](#)), that are known to be present in the clouds of Uranus, are therefore also present within the atmosphere, however, following HM80 we continue to assume that these are in negligible proportions relative to H₂ and He. They move on to use data from Monte Carlo models to determine the behaviour of the materials at higher pressures, fitting to polynomials of which we utilise the coefficients seen in their Table 1.

Cold curve data is used to further take into account contributions of the how the specific internal energy of the material changes while at $T = 0K$. This adds an energy contribution from the structural effects of the material of,

$$u_0(\rho) = \int_{\rho_0}^{\rho} \frac{P_0(\rho)}{\rho^2} d\rho, \quad (6)$$

that can then be added to the thermal component as,

$$u(\rho, T) = u_0(\rho) + C_V T, \quad (7)$$

where C_V is the specific heat capacity at constant volume for the material (Kegerreis et al., 2018).

2.1.3 Stability Criteria

Stability criteria are the basis from which one can describe fluid motion as being described by convective motion or otherwise. This considers an adiabatic fluid element within a superadiabatic planetary interior. In this situation we have a fluid parcel that when moved towards the surface has a higher temperature and lower density than its surroundings. Hence with a superadiabatic interior profile, the element moves upwards until it reaches a boundary where it can deposit heat and consequently sinks down until it reaches a heat source and then rises again. Through this transfer of heat via convective motion, the interior tends towards an adiabatic temperature gradient (Glatzmaier, 2014).

Assuming a homogeneous interior, i.e an interior consisting of a mean molecular weight logarithmic gradient towards the centre of the planet of $\nabla_\mu = 0$, the Schwarzschild (1906) criterion is utilised such that

$$\nabla_T - \nabla_{ad} = \left(\frac{\partial \ln T}{\partial \ln P} \right) - \left(\frac{\partial \ln T}{\partial \ln P} \right)_{ad} > 0 \quad (8)$$

where ∇_T is the logarithmic temperature gradient and ∇_{ad} is the corresponding adiabatic temperature gradient (taken at constant entropy). If this is satisfied, then the fluid is unstable to fluid motion and hence it possesses convective motion (Leconte & Chabrier, 2012).

Nonetheless, this only holds true for a homogeneous interior, which is not realistic for planetary models. Instead, one must consider a positive mean molecular gradient such that $\nabla_\mu > 0$. Therefore, the instability criterion is further developed to include this factor through the Ledoux (1947) criterion,

$$\nabla_T - \nabla_{ad} > \nabla_\mu, \quad (9)$$

where we now include ∇_μ , the logarithmic mean molecular weight gradient. This can also be written in full as

$$\left(\frac{\partial \ln T}{\partial \ln P} \right) - \left(\frac{\partial \ln T}{\partial \ln P} \right)_{ad} > \left(\frac{\partial \ln \mu}{\partial \ln P} \right). \quad (10)$$

2.1.4 Internal Fluid Structures

Considering fluid structures created from large scale motion of particles can advance models of heat transfer and cooling. Including these structures allows consideration of how these impact on the heat transfer efficiency and may explicitly show diffusive layers preventing heat transfer from the interior as discussed by Podolak et al. (1991); Podolak et al. (1995).

Structures can be classified within several groups as described in Leconte & Chabrier (2012, henceforth LC12). These are briefly described below and are known as 'overturning convection',

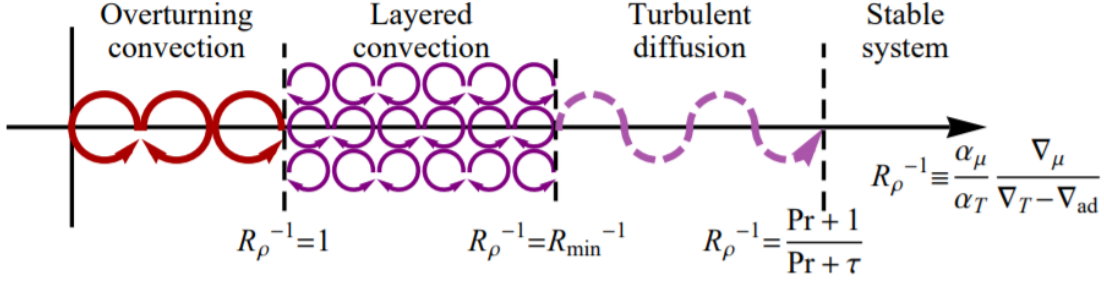


Figure 1: Diagram from LC12 to illustrate the different fluid structures from overturning convection, with large scale heat transfer, through to turbulent diffusion, which is much less efficient, tending towards a stable system.

'layered convection', and 'turbulent diffusion', heading from large scale convection towards a stable system with diffusive motions. The type of fluid motion can be determined by using R_ρ , the density ratio defined by,

$$R_\rho = \frac{\alpha_T}{\alpha_\mu} \frac{\nabla_T - \nabla_{ad}}{\nabla_\mu}, \quad (11)$$

where α_T and α_μ are described by,

$$\alpha_T \equiv -\frac{\partial \ln \rho}{\partial \ln T} \Big|_{P,\bar{\mu}} \quad , \quad \alpha_\mu \equiv \frac{\partial \ln \rho}{\partial \ln \bar{\mu}} \Big|_{P,T}. \quad (12)$$

The density ratio has distinct regions assuming a mean molecular gradient of $\nabla_\mu > 0$ such that ∇_μ increases towards the centre of the planet as expected. A useful diagram to illustrate this is shown in Fig 1 of LC12, shown here in Fig 1.

For 'overturning convection', large convective cells are created within the material. Both the Ledoux and Schwarzschild criteria for instability are satisfied resulting in large cells. Here the mean molecular gradient is insufficient to affect the shape of size of these cells, and this correlates to an inverse density ratio $R_\rho^{-1} < 1$ (LC12).

'Layered convection' is then defined as a series of layers of smaller convective cells. The size of these is determined by the mean molecular gradient and is stable by the Ledoux criterion but not by Schwarzschild.

As the molecular gradient becomes larger still, the regime moves towards that of 'turbulent diffusion', whereby a diffusive state takes over and convective processes are no longer present.

Since diffusive heat transfer is shown to have less effective heat transfer relative to the convective case, as [Podolak et al. \(1991\)](#) suggested, a series of diffusive layers would effectively prevent heat from the interior of the planet from reaching the surface.

2.1.5 Clouds and Condensation

Clouds within the atmosphere of Uranus have continued to be researched from Earth thanks to advances made in ground and space observations, for example with the Very Large Telescope and the Hubble Space Telescope ([de Pater et al., 2015](#); [Irwin et al., 2015](#); [Irwin et al., 2016](#)).

The presence of these structures leads one to ask whether they have any significant influence on the flux in and out of the planetary surface. These clouds, located primarily in the upper troposphere, are predominantly formed of CH₄ and clouds of H₂S are also known to form in the mid troposphere (Fletcher et al., 2019). It should be reiterated here that although the clouds are mostly formed of CH₄, this only makes up 2.3% of the atmosphere (Lindal et al., 1987) and so is deemed negligible as in HM80 for the EoS. If formed on a significant surface area of the planet, clouds have the possibility of altering the albedo of the planet such that large cloud coverage leads to a higher albedo and hence higher reflection of the solar flux incident on the surface. For Uranus, Hanel et al. (1986) determine the clouds to be of negligible size to influence the albedo of Uranus determined by Voyager in Pearl et al. (1990).

2.2 Simulation Methods

To investigate whether the giant impact hypothesis is capable of explaining the heat flux we observe, we run a pair of simulations within which a proto-Uranus and impactor collide. The simulations, their parameters and initial conditions are detailed.

2.2.1 Smoothed Particle Hydrodynamics (SPH)

In order to perform these impact simulations, 3D smoothed particle hydrodynamics (SPH) was utilised. SPH is a Lagrangian method to solve the equations of fluid dynamics, smoothing over neighbouring particles for average values at each point. For this we compute the density of particles using a kernel weighted sum described by

$$\rho(\vec{r}) = \sum_{j=1}^{N_{neigh}} m_j W(|\vec{r} - \vec{r}_j|, h), \quad (13)$$

where W is the smoothing kernel, which describes the weighting function of the surrounding particles, and h is the smoothing length.

For a physical understanding of the SPH equations, a 3D Gaussian kernel is most suitable,

$$W = \frac{1}{(\sqrt{\pi}h)^3} \exp\left(\frac{r^2}{h^2}\right). \quad (14)$$

This provides a weighting of the particles such that the contribution decreases with radial distance. The smoothing length, h , effectively determines the range of this Gaussian kernel such that there is a limit to the number of neighbours considered in the calculation. This prevents a tendency to include particle contributions at infinity, reducing the calculation time (Price, 2012; Monaghan, 1992). A maximum smoothing length, h_{max} , is also used and set to be 0.1R_U, such that the averaging is computed on adequately small scales to carefully resolve substructure and to prevent these regions reaching scales of the order of $\sim R_U$.

2.2.2 SWIFT

These SPH simulations were performed with SWIFT (SPH With Inter-dependent Fine-grained Tasking, version 0.8.5). SWIFT is a SPH solver designed to take advantage of the thousands of nodes which make up modern-day supercomputers, allowing for faster, higher resolution simulations, and is available at swift.dur.ac.uk/. This is used on 1 node with 24 cores on the Hamilton Cluster, part of the High Performance Computing Service, to run the simulations.

2.2.3 Planetary Profiles

The interior planetary profiles can be derived ensuring hydrostatic equilibrium and mass conservation in the planet. For a non-rotating planet, hydrostatic equilibrium takes the form

$$\frac{dP}{dr} = -\frac{GM(< r)}{r^2}\rho, \quad (15)$$

where dP and dr are the change in pressure and radial distance, G is the gravitational constant, M is the mass enclosed and r is the radius. Mass conservation is applied ensuring

$$dM = 4\pi r^2 \rho dr. \quad (16)$$

A non-rotating planet is used to ensure simplicity of the hydrostatic equilibrium in this instance. To compute the interior profile requires integration inwards from the outside where we have initial boundary conditions such as the surface temperature and pressure, from which the change in pressure over this layer, dP , can then be calculated from the hydrostatic equilibrium equation. For this constant density in the layer is assumed and hence integrating over small increments is more desirable. From the pressure value determined, new temperature and density values can be computed from the EoS given as described in Section 2.1.2. This allows us to continue the integration inwards whilst describing the behaviour of the material within each layer.

Checks are implemented to ensure that as we conduct this integration, there is neither a surplus of mass left in the interior of the planet, nor a deficit in which case the resulting planet would be non-physical with a hole in the centre. For this, consideration of where the boundaries between the different material layers are placed is important. This is easier for the two-layer impactor models as typically this is done by integrating inwards and if there is an excess of mass in the core left over, the boundary is incremented outwards. This is repeated until the mass left in the core of the planet is below a set value.

Applying this for three-layer models results in potential degeneracies in the position of boundaries as multiple pairs of boundaries at different radii could satisfy the above requirements. Instead, here we must take into account the moment of inertia, if known from gravitational moments, of the planet to remove at least some of these. This comes in as an additional criterion to satisfy and it can be computed using the definition of the moment of inertia,

$$I = \int r^2 dm = \int_0^R 4\pi r^4 \rho(r) dr. \quad (17)$$

This can also be applied to the two-layer models if there is a certain moment of inertia value that is desired.

Object	Mass [M_{\oplus}]	Radius [R_{\oplus}]	Temperature [K]	Pressure [bar]	I/MR^2
U-1	12.436	4.0	60	1.0	0.21
U-2	11.436	3.97	60	1.0	0.21
I-1	2.0	2.05	270	2000.0	0.23
I-2	3.0	2.25	270	2000.0	0.23

Table 1: Overview of the target and impactor specifications are detailed. A horizontal line has been added to divide the Uranus profiles, denoted with 'U', to the impactors, 'I'. The temperature and pressure values both refer to the surface values.

Planetary bodies as in Table 1 are created and the profiles are illustrated in Fig 2. The profiles for temperature and pressure should be continuous throughout the planet, as can be seen in Fig 2 where the only discontinuities present are those in the density profile. This is a consequence of assuming homogeneous layers of the planet such that there is no mixing between the materials presented for each layer which have different EoS. The surface temperature is taken to be the present-day temperature since the temperature at which an impact had taken place is unknown, in addition to another unknown in the temperature of the mid-plane of the protoplanetary disc where planets form (Kurosaki & Inutsuka, 2018). The layers of the planets are assumed to have an isothermal rocky core and adiabatic icy mantle and atmosphere following from HM80.

2.2.4 Initial Conditions

For these simulations, particle distributions for the target and impactor needed to be constructed and the impact parameters set. The composition of the impactor and target's profiles is taken into account using the module SEAGen (Kegerreis et al., 2019). This can place particles of various material types in two and three layer model spheres, using density profiles created to consider the mass and composition of various objects. Using this module, particle distributions for a Uranus model and corresponding impactors of various compositions can be made and set to run within SWIFT. An in-depth discussion of SEAGen can be read in Kegerreis et al. (2019).

Once these initial profiles were created, they were run in SWIFT to allow the particles to settle to their natural positions in the sphere assuming no initial velocities to the particles. Tracking this forwards in time we can observe how the various energies within the simulation change and we use a criterion to determine at what point the sphere has 'settled'. The standard definition for a 'settled' profile is that the root mean square velocity, $v_{rms} \sim 0.01v_{esc}$, where for a Uranus profile of $R_U = 3.98R_{\oplus}$ and $M_U = 14.5M_{\oplus}$ we have $v_{esc} = 21.3$ km/s. The time expected for the planet to settle is given as the time it takes for one complete oscillation of a sound wave through the planet and back, similar to estimating stellar pulsation periods. For all profiles run this resides in the interval $\sim 12000 - 13000$ s in the physical time of the simulation. Testing this within the settling simulations shows that for the I-1 impactor with $v_{esc} = 11$ km/s this value of $v_{rms} = 0.1$ km/s can be reached within the first saved timestep at 1000s in simulation seconds. An example of the energy variations throughout this 'settle' simulation can be seen in Fig 3. It should be noted that despite the settle criterion above, the impactor is deemed as settled far earlier than the predicted settle time using the sound speed oscillation through the

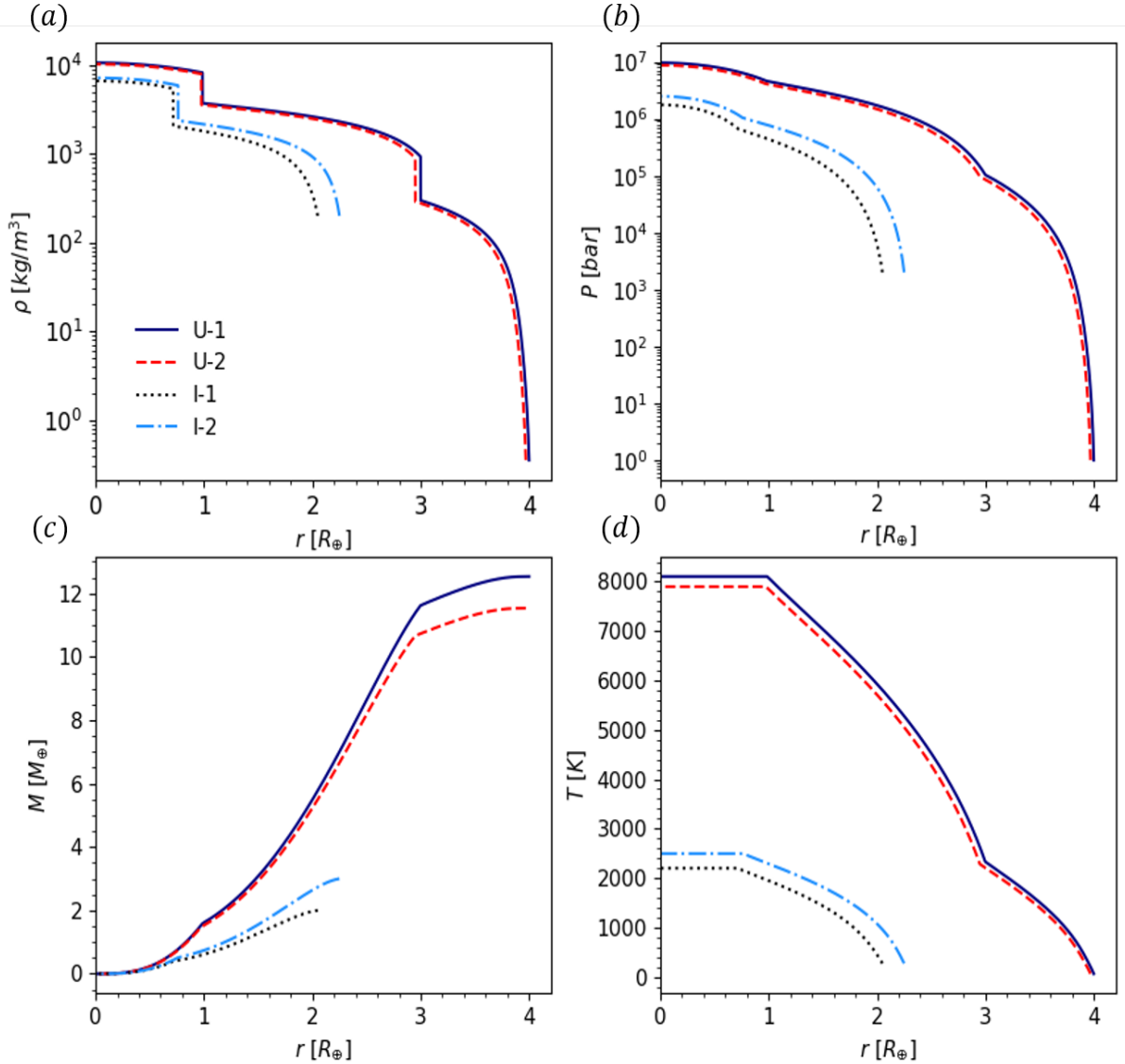


Figure 2: Interior planetary profiles for the targets and impactors as in Table 1 is shown. a) Depicts the density as a function of radius, using the HM80 equations of state for the atmosphere, icy mantle and rocky core. b) Shows the the interior pressure with radius, c) shows the cumulative mass distribution and finally, d) shows the temperature as a function of radius. The pressure and temperature profiles are clearly continuous as is expected while the discontinuities in (a) for the density appear due to the changing material within the different layers.

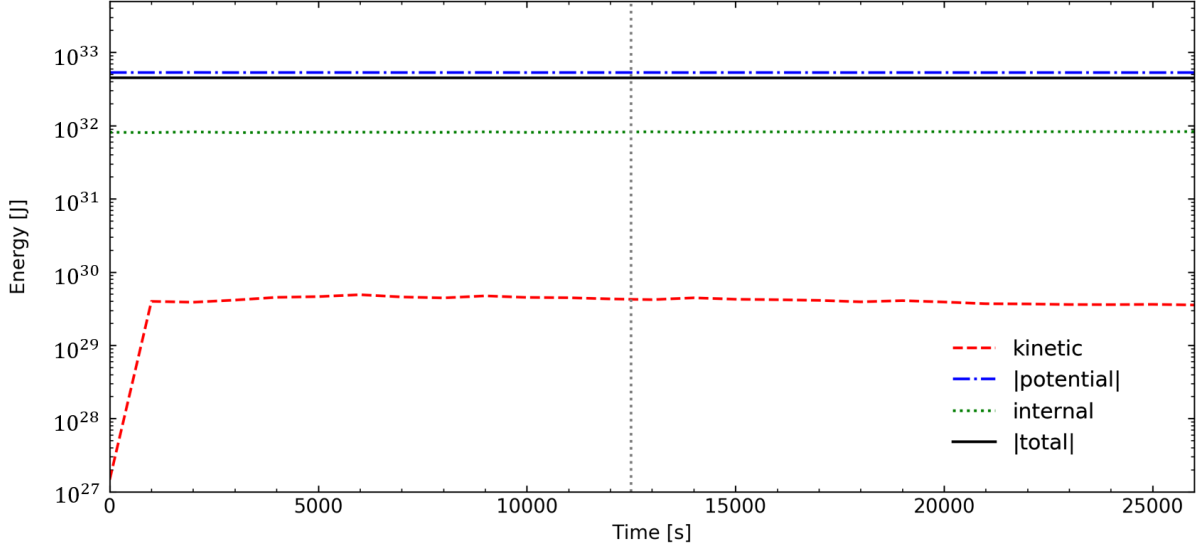


Figure 3: Variation in kinetic, potential and internal energies of the settle simulation for the I-1 impactor. The total energy at each timestep is plotted to show this is constant throughout. The absolute values of the total and potential are used to more easily compare the magnitudes and variations. A vertical line has also been added at the point of expected settling from the sound wave oscillation at ~ 12500 s but it is clear that the planet has settled far earlier, around ~ 1000 s.

planet. A further check on this can be obtained by plotting the settled planet profiles, comparing them against the profile created initially when deriving the planetary interior profiles as in Fig 4. Absolute deviations are derived from the data in each case using,

$$D = \frac{1}{N} \sum_{i=1}^N |x_i - m(r)|, \quad (18)$$

where D is the absolute deviation, x is the settled simulation value for each i particle included in the deviation calculation, $m(r)$ is the expected value from the initial profile at the same radius as the x_i value to take into account varying values in each profile with radius and N is the number of points taken into consideration.

Using this definition, absolute deviations are calculated to be 68.6 kg/m^3 in density, corresponding to a value in the atmosphere of the planet and more two magnitudes less than that of the rocky core density values. For pressure, a value of $1.0 \times 10^5 \text{ bar}$ is calculated, a magnitude similar to the pressure at the boundary between the atmosphere and mantle. Finally for the specific internal energy, the absolute deviation is $1.0 \times 10^6 \text{ J/kg}$, lower than the smallest value in the simulation by almost a magnitude. Blips in the pressure values calculated are observed in the simulation data at the boundaries between material layers. This is a consequence of contact discontinuities where the jumps in density values don't receive special treatment and is likely to increase the absolute deviation value (Price, 2008). These settled planets are then used in the next section where the collision simulations are set up. There will be additional time at the start of the collision simulations prior to impact for the profiles to further settle so these deviations are not seen as significant.

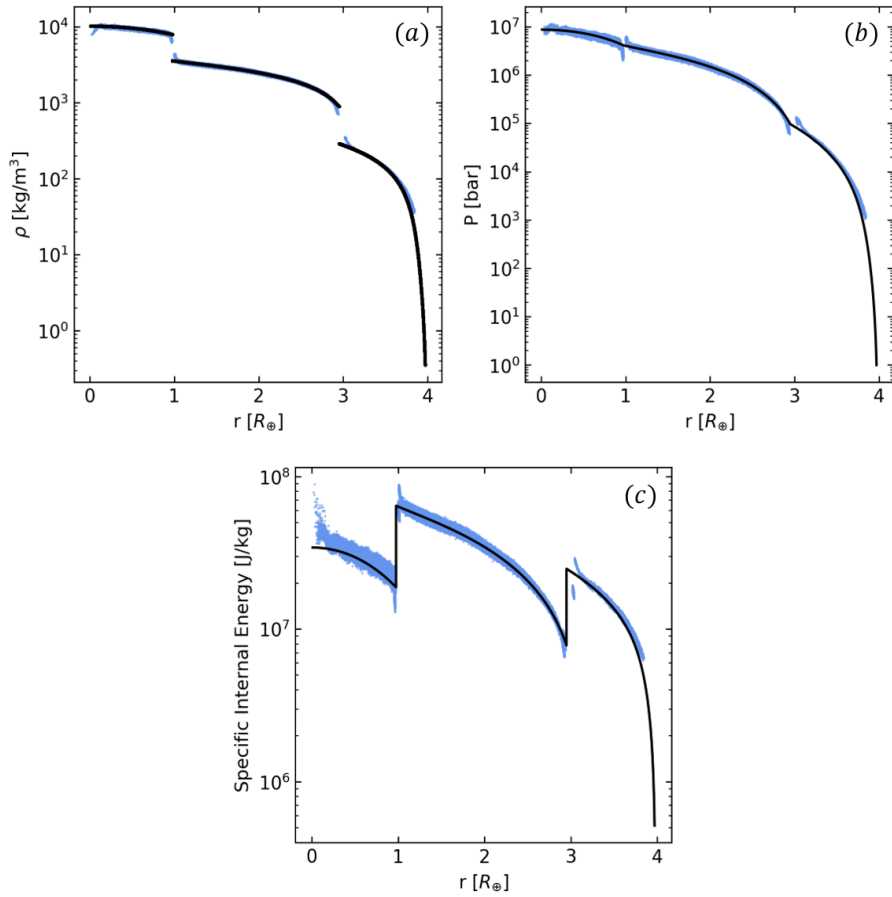


Figure 4: Checking the deviation from the initial profiles for the U-2 profile that has been 'settled' for ~ 13000 s, which is the profile later used in the collision simulation. In (a) the density profile is shown; in (b) the pressure profile and finally in (c) the specific internal energy profile. The black line shows the initial planetary profile while the blue data points are individual particles from the simulation at the timestep chosen. Only small deviations from the initial profiles are seen with absolute deviations in each settled profile of 68.6 kg/m^3 in (a), $1.0 \times 10^5 \text{ bar}$ in (b), and $1.0 \times 10^6 \text{ J/kg}$ in (c).

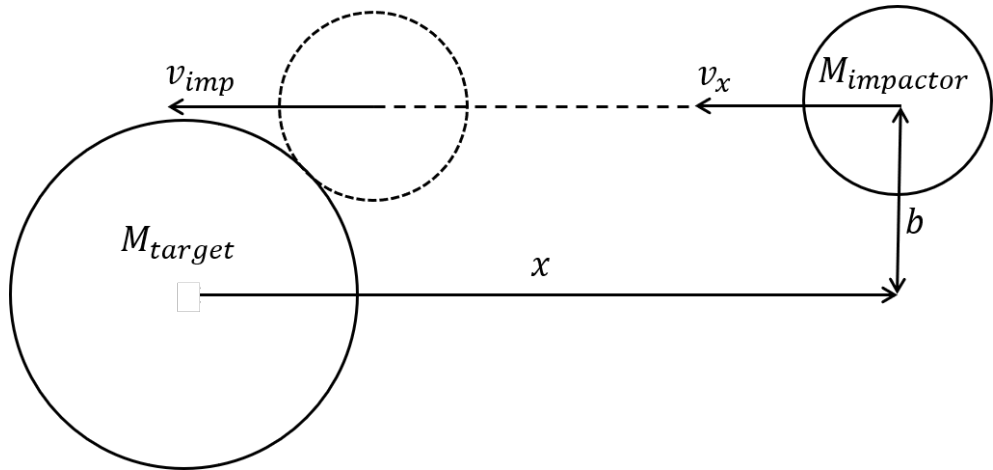


Figure 5: Schematic of initial set-up of simulation showing the impactor and target. The parameters are detailed as follows: x is the initial separation of the target and impactor in the x direction, b is the 'impact parameter', v_x the initial velocity and v_{imp} the impact velocity.

2.3 Details of Simulation Runs

For Uranus, a three-layer model was chosen to describe its composition. This followed that of HM80, comprising of a rocky core, icy mantle and atmosphere, each represented with particles having a material flag that can be traced throughout the simulations. The corresponding EoS for each material layer is described in Section 2.1.2. For the impactors, bodies formed of a rocky core and icy mantle at $2M_{\oplus}$ and $3M_{\oplus}$ are chosen as these were shown in [Kegerreis et al. \(2018\)](#) to be able to recreate the obliquity and rotation rate of Uranus, whereas a $1M_{\oplus}$ was shown to be insufficient. Using the assumption that there is minor mass lost from the system the corresponding proto-Uranus mass in these simulations is $M_U = 14.436M_{\oplus} - M_I$, where M_I is the mass of the impactors as above.

The simulations ran focus on scenarios that have been shown to create merging events with sufficient angular momentum to recreate the present-day rotation rate (17.24hrs, ([Warwick et al., 1986](#))) following from [Reinhardt et al. \(2019\)](#) and [Kegerreis et al. \(2018\)](#). This results in simulations with an impact parameter $b = 0.7$ which [Reinhardt et al. \(2019\)](#) showed to ensure merging, and not hit-and-run events. The impact parameter is described as the perpendicular distance between the velocity of the impactor and the centre of the target, and the impactor velocity as the velocity at the point of contact between the two bodies. The impact velocity is calculated from $v_{imp} = \sqrt{v_{esc}^2 + v_{\infty}^2}$, where v_{imp} , v_{esc} and v_{∞} are the impact velocity, escape velocity and velocity at infinity. The escape velocity is calculated for each proto-Uranus and the impact velocity is calculated as in [Reinhardt et al. \(2019\)](#) assuming that $v_{\infty} = 5\text{km/s}$ for each impactor, resulting in the impact velocities on contact as in Table 2.

The initial separation, r , of the bodies is determined by calculating the distance at which the gravitational force on the surface of the impactor from the impactor itself is 10 times as strong as that of the target planet. This allows for more physical simulations with tidal forces of the bodies to be included as they approach instead of setting the particles at the position of impact itself. The x separation can then be determined from $x = \sqrt{r^2 - y^2}$, where $y = bR_U$, and the velocity at infinity here is set to the $-x$ direction.

In general, these were run containing a total of 10^6 particles for 100,000s $\sim 28\text{hrs}$ in simulation time to allow for the impact to occur and for the planet to evolve with sufficient time to settle again afterwards. Minimal and maximal timesteps of 10^{-6}s and 1000s were used to ensure that each timestep was accurately run. Similar to simulations run by [Reinhardt et al. \(2019\)](#), the distribution of these particles between the target and impactor was determined such that the mass of each particle, regardless of the body of origin, would have similar masses resulting in particle masses of $\sim 1.4 \times 10^{-5} M_{\oplus}$ or in kg, $\sim 8.4 \times 10^{19} \text{kg}$ each. Although the number of particles here is not as large as 10^8 in [Kegerreis et al. \(2019\)](#), this choice was limited due to time restraints within the duration of the project, and may lead to problems regarding the accuracy of results. Consideration of the convergence of results, examining particle numbers used in these simulations, is described in Section 4.4. The simulation parameters are detailed alongside the particle number of each impactor and target in Table 2.

Sim.	Impact Parameter (b)	Impact Velocity [km/s]	Target Particles	Impactor Particles
U-1	0.7	20.1	8.6×10^5	1.4×10^5
U-2	0.7	19.4	7.9×10^5	2.1×10^5

Table 2: Parameters of the simulations run, describing values chosen for the impact parameter, impact velocity at contact, and target and impactor particle numbers. Each simulation uses the pair of impactor and target with the same number, i.e simulation 1 uses U-1 and I-1, as was previously described in Table 1.

3 Results

From the previously described simulations we examine the simulation as it evolves throughout the impact and post-impact. In particular, the distribution of the impactor material and how the internal energies vary in time are examined.

3.1 Particle Distribution

As we aim to consider whether it is plausible to create diffusive interfaces from the impactor's core material on the proto-Uranus' core, an investigation is initially conducted into where this material is placed.

Firstly, by altering the colour of the impactor's core to be in high contrast to the surrounding material, it can be seen in Fig 6 that this can settle around the proto-Uranus' core by the end of the simulation time in both simulations. The mixing of impactor material into the planet during the impact is also depicted by showing the evolution of the simulation over several timesteps. It is clear that there is sufficient impactor material accumulated in layers of the proto-Uranus, illustrating the potential within these simulations to create the composition gradient necessary to create diffusive interfaces.

3.1.1 Impactor Radial Placement

More quantitative values of the distribution are desirable. For this Fig 7 shows greater detail in these final positions at ~ 27 hrs for the U-1 simulation, forming two distinct distributions in the final positions of the core and mantle of the impactor in the proto-Uranus. In the following, where the distribution of the impactor material is investigated more thoroughly, the 'core' and 'mantle' refer to the impactor's material exclusively.

For the U-1 simulation the mean radial position for each group is $\bar{r}_{core} = 1.014 \pm 0.001 R_{\oplus}$ for the core and $\bar{r}_{mantle} = 3.396 \pm 0.006 R_{\oplus}$ for the mantle, with standard deviations of $\sigma = 0.196 R_{\oplus}$, and $\sigma = 2.213 R_{\oplus}$ respectively. With this spread in the mantle distribution, the lower 1σ value lies just inside the upper 1σ value for the core but not into the peak of the histogram of the core positions. Although a larger bin number has been chosen for the mantle particles given the wider spread, this does not appear to present any further detail in the distribution of the mantle in the proto-Uranus and a somewhat uniform placement with radius is implied. The larger spread in the mantle distribution of a factor of 11 to the standard deviation of the core is likely in part to be due to a larger proportion of these particles which are effectively lost from the planet during

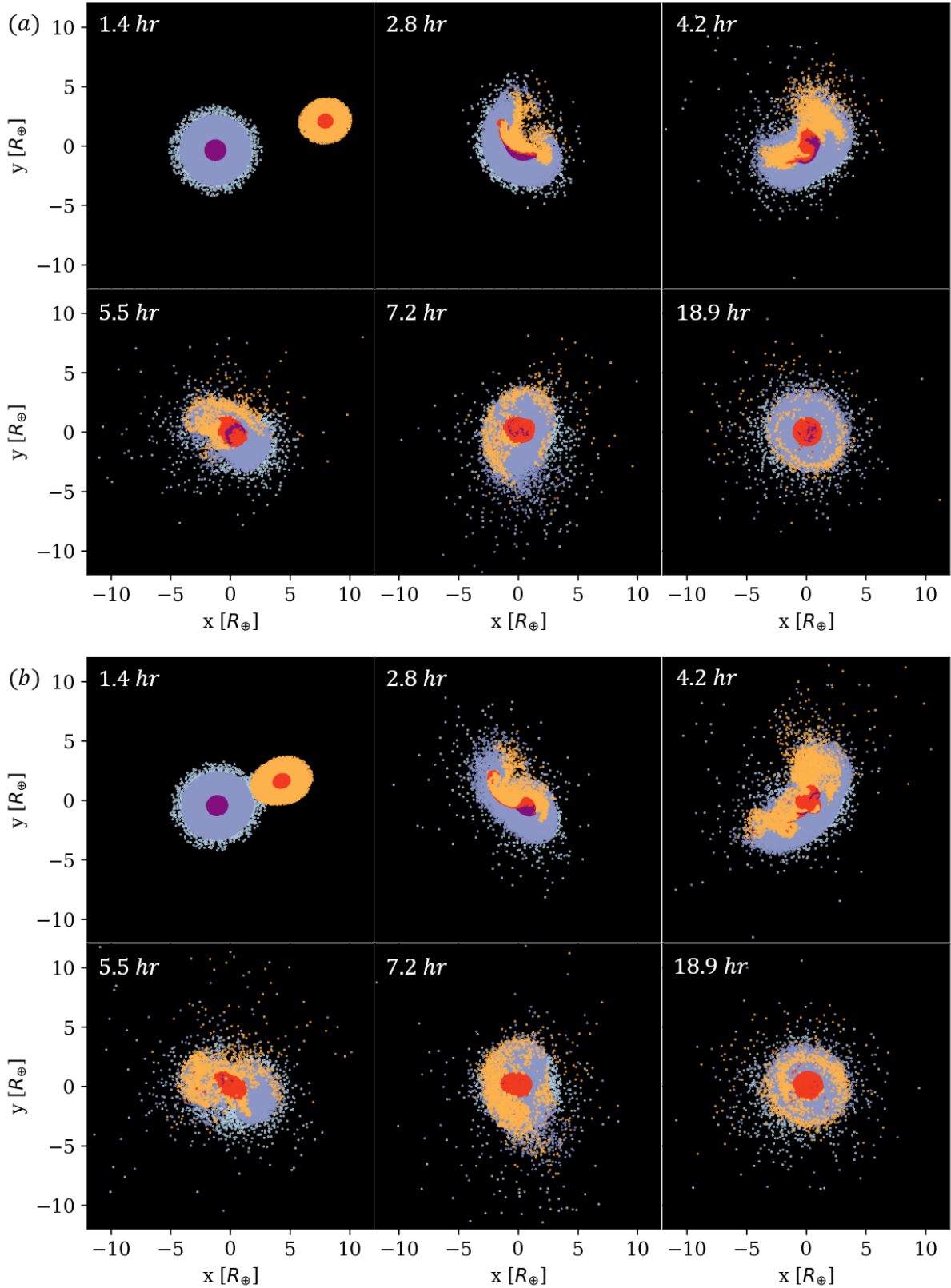


Figure 6: Snapshots of the impact simulations of (a) U-1 and (b) U-2. In each simulation, a range of timesteps are chosen illustrating the detail and evolution of the simulation. The U-2 simulation appears to have a more violent impact with more mixing of the impactor's material in the proto-Uranus by the final timestep, however, both have final distributions with sufficient impactor material distributed around the core. As the impactor core material is plotted last, this appears to completely cover the core in some snapshots.

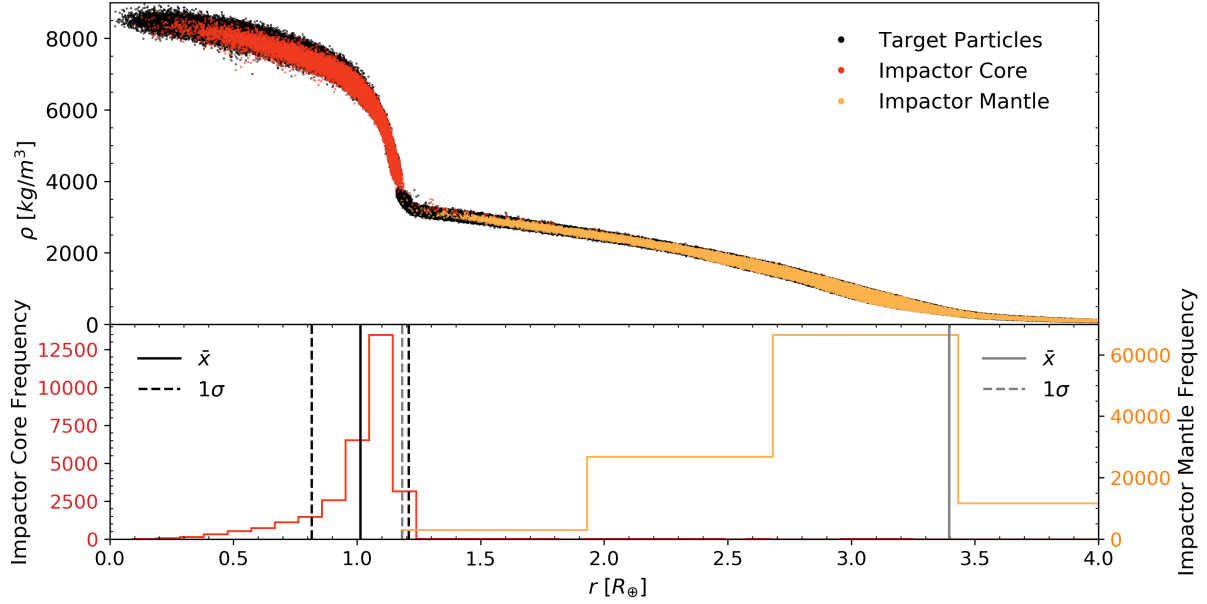


Figure 7: Density profile with radius illustrating particle positions at 98000s ~ 27 hrs for the U-1 simulation. The proto-Uranus particles are plotted in black, and the impactor particles have been split into red for core, and orange for mantle. Below are the corresponding histograms for the impactor core and mantle distributions. Vertical lines have been added in black and grey, for the impactor core and mantle respectively, to highlight the spread in data with the mean and one standard deviations plotted. In addition to showing the different placement of these particles at the end of the simulation, standard deviation values illustrate the factor of 11 increase in spread for the mantle distribution compared to the core. A similar shape, albeit with greater spread, is obtained for the U-2 simulation.

the impact but remain within the box of our simulation.

For the U-2 simulation, the two groups of particles again have distinctive spreads. The mean radial positions are $\bar{r}_{core} = 1.041 \pm 0.003R_{\oplus}$ and $\bar{r}_{mantle} = 3.263 \pm 0.008R_{\oplus}$, with a larger spread in both groups to the U-1 results with standard deviations of $\sigma = 0.445R_{\oplus}$ and $\sigma = 2.688R_{\oplus}$. This suggests that more massive impactors, with smaller targets as a result of assuming the objects sum to the same final mass, result in more violent collisions.

To determine the proportion of particles which leave the system the fluid satellite definition of the Roche radius of a planet,

$$r_R = (16)^{\frac{1}{3}} \left(\frac{\rho_U}{\rho_m} \right)^{\frac{1}{3}} R_U = (16)^{\frac{1}{3}} \left(\frac{3M_U}{4\pi\rho_m} \right)^{\frac{1}{3}}, \quad (19)$$

is used as a boundary. The second term above arises from using $M = \frac{4}{3}\pi\rho_U R_U^3$, where ρ_U is the density of Uranus which is variable with radius, hence the substitution to mass. ρ_m is the density of the material considered, for which the average densities of the impactor's core material and mantle material for the U-1 simulation are determined to be $6.1 \times 10^3 \text{ kg/m}^3$ and $1.0 \times 10^3 \text{ kg/m}^3$. The roche radii for these are then calculated to be $r_R = 5.95R_{\oplus}$ for the core material and $r_R = 10.78R_{\oplus}$ for the mantle. For the U-2 simulation we retrieve average densities of $5.7 \times 10^3 \text{ kg/m}^3$ and $1.3 \times 10^3 \text{ kg/m}^3$ with corresponding roche radii $r_R = 6.09R_{\oplus}$ for the core material

and $r_R = 10.03R_{\oplus}$ for the mantle.

Using this definition, none of the impactor's core material has left in the U-1 simulation while for the impactor's mantle 0.3% of the material moves beyond this boundary. Conversely, in the U-2 simulation, in addition to the increased spread in radii at the final positions, 0.1% of the core and 0.5% of the mantle move beyond their respective roche radii. As particles that move outside the boxsize of the simulations, $100R_{\oplus}$, are removed, this value should be taken as a lower estimate.

3.1.2 Impactor Core Coverage

Considering the impactor's core material within the proto-Uranus as a candidate to create the all-important diffusive interfaces, further analysis into the coverage of this material around the core is beneficial. From Fig 7 we determined the average position of the impactor's core to be focused at the core-mantle boundary of the proto-Uranus. Hence, the particles spanning radial positions $(\bar{r}_{core} - \sigma) - (\bar{r}_{core} + \sigma)$ in each simulation are chosen for this investigation.

Assuming each particle is uniformly spherical in shape with radius r_p , this radius value can be calculated for each particle using the mass, m_p , and density, ρ_p , through rearranging $m = \frac{4}{3}\pi\rho_p r_p^3$. Further assuming the coverage of each particle takes the form of a circle, the total coverage in a layer of the planet can be found by summing the particle areas. Completing this for all particles within the 1σ boundaries for the U-1 impactor's core material, the complete coverage is calculated to be $44.6R_{\oplus}^2$, 3.5 times larger than the value for the surface area of a shell taken at \bar{r}_{core} of $12.8R_{\oplus}^2$. For U-2 the total coverage is $62.2R_{\oplus}^2$, 4.6 times larger than the surface area of a shell taken at \bar{r}_{core} of $13.6R_{\oplus}^2$.

Since this value for the whole interval is far greater than the surface area of a sphere at the core-mantle radius, smaller intervals within this are then investigated in turn, with even intervals within the standard deviation values to compare coverage in each simulation. This can be seen in Fig 8. In particular, the highest coverage is seen in both simulations between $1.12R_{\oplus}$ and $1.17R_{\oplus}$, with the highest coverage in the U-1 simulation of 78% and 67% in the U-2 simulation. It should be warned here that the percentage coverage of the shell surface area assumes that the particles are not overlapping within the radii bounds which is unlikely in reality.

By making the radial intervals smaller we can examine the extend to which particle areas are overlapping and correct our coverage values in line with this. A method to check this overlapping directly is to map areas of particle coverage onto a 2D plane. This can be done by converting the Cartesian coordinates into spherical polars to determine the latitude and longitude values, which are then projected into a 2D plane. This can be done using various map projections from a sphere, however, in order to retain the relative sizes of the area coverage of particles to the sphere surface area, a Gall-Peters projection is used. This projection maps areas to have the same relative sizes to each other and as such, the final mapping has an area corresponding to a sphere surface $4\pi r^2$ ([Gall, 1885](#)). The projection provides x and y values that can then be plotted in a rectangular plane. These values are found using the longitude, λ , and latitude values, φ , from our spherical coordinates, and the radius of the sphere, R , with the following equations,

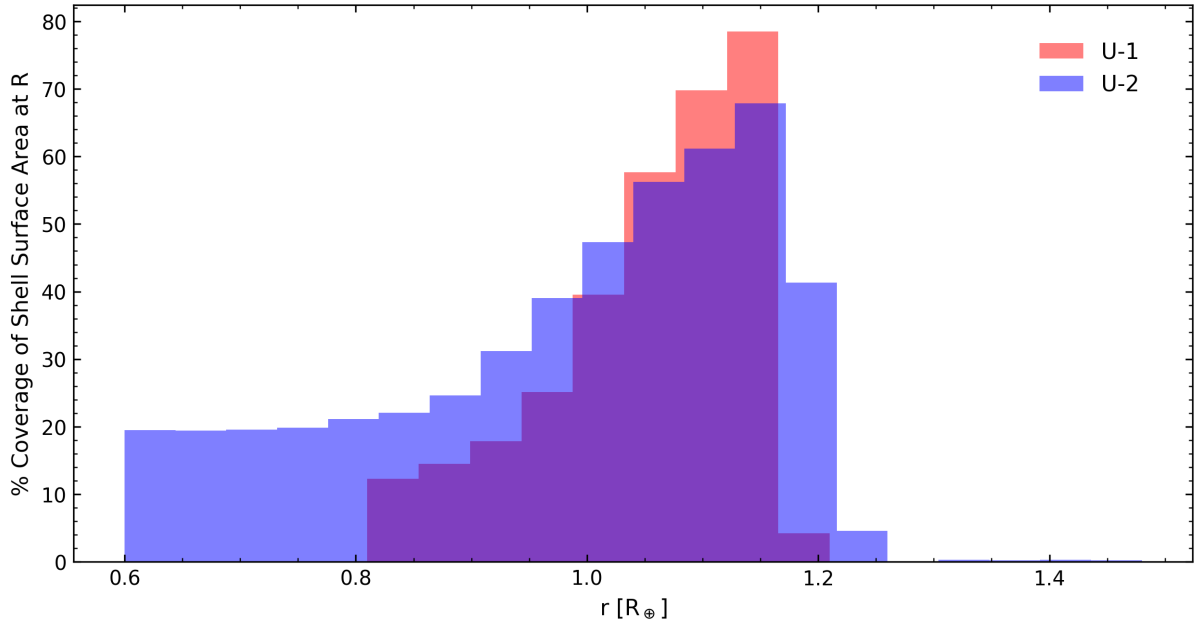


Figure 8: Percentage coverage of surface area of shells with impactor core material between radial values within the lower and higher standard deviations of the core material at the end of each simulation. U-1 and U-2 are shown in red and blue showing that significant areas of the planet can be covered around the core-mantle boundary.

$$x = \frac{R\pi\lambda\cos(45^\circ)}{180^\circ}, \quad (20)$$

$$y = \frac{R\sin\varphi}{\cos(45^\circ)} = R\sqrt{2}\sin\varphi. \quad (21)$$

The x and y values are found and plotted for five radial intervals within the peak coverage for each simulation from Fig 8. A series of these snapshots from the second simulation can be seen in Fig 9 in addition to the two 'master maps' created for the simulations combining their smaller interval frames together.

Overlapping can clearly be seen in the master maps and calculating the areas covered in this instance returns coverage values of 72% for the U-1 simulation and 65% for U-2. This demonstrates that, as expected, overlapping does occur when calculating total areas covered within a radial interval larger than the particle radius, however, the areas computed here are only 7.7% and 3.0% different from their original values. This suggests that we can still achieve a high proportion of surface coverage at the peak radial interval for coverage. Further work will be necessary to determine the influence of this on the heat flux, and the properties of this coverage required to inhibit heat flux.

3.2 Internal Energies

It is also important to consider the energy distribution of the particles throughout and at the end of the simulations since this may highlight key points of interest when investigating the heat flux

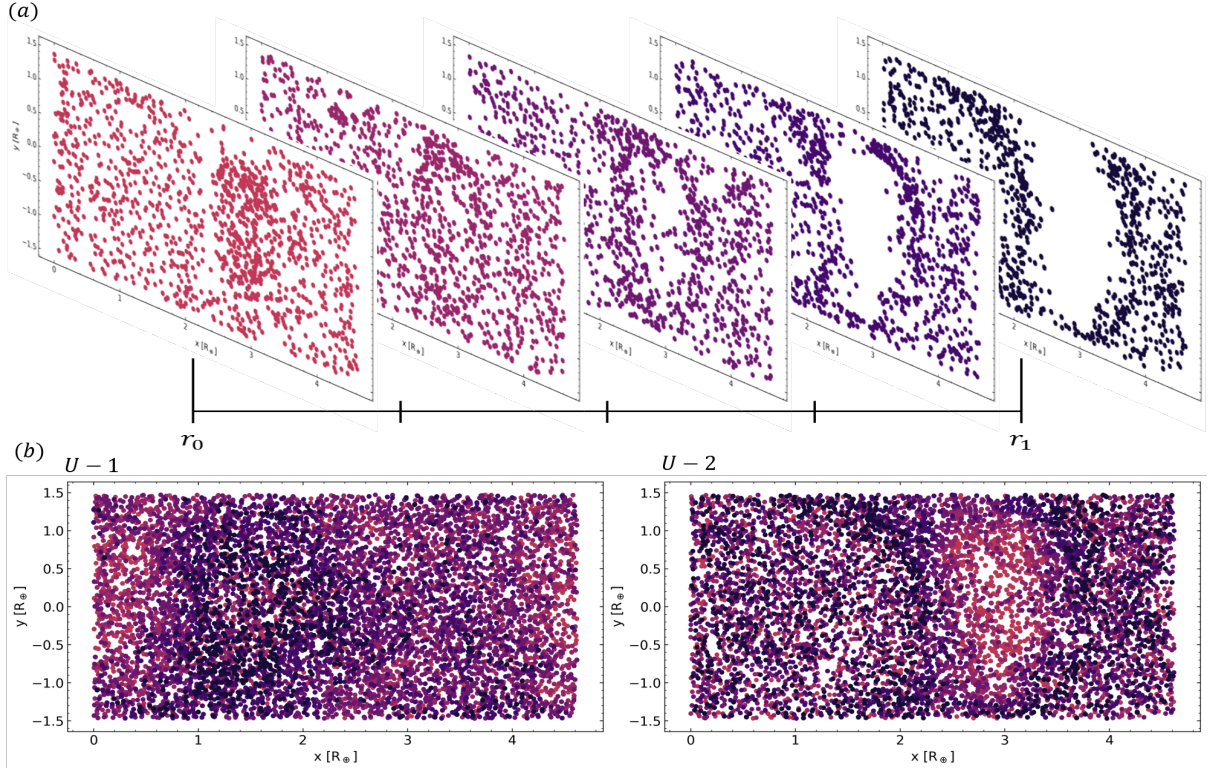


Figure 9: (a) Shows a series of mapped particle areas from within the peak coverage radial interval of Fig 8 for the U-2 simulation. Sequential colours are used to show different shells which are consequently superimposed together to make the master plots which are shown in (b).

from the planet. For example, it may be the case that the impact can create accelerated cooling as in [Kurosaki & Ikoma \(2017\)](#), by dredging up materials from the inside of the planet, and as a consequence higher internal energies might be observed for particles on the edge of the planet.

Fig 10 shows the changing specific internal energies throughout a selection of snapshots from each simulation. The transfer of kinetic energy to thermal energy of the particles at the point of collision can be seen in bright points indicating higher internal energy values at the impact location and into the planet. Additional heating can be seen in later times, potentially as a consequence of mixing of the different components of the impactor material into the proto-Uranus as the simulation evolves.

More particles towards the edge of the planet in the 5.5hr and 7.2hr snapshots also show higher specific internal energies. Perhaps these could suggest enhanced plausibility for the accelerated cooling as in [Kurosaki & Ikoma \(2017\)](#), or at least a short period of this behaviour as the final snapshot in Fig 10 for the U-2 simulation appears to have globally lower internal energies compared to the earlier snapshots mentioned. On the other hand, U-1 continues to have particles with higher internal energies on the outside of the planet in the last snapshot indicating that the lower mass impactor may have heat radiated in this way for longer time periods than the $3M_{\oplus}$ impactor in U-2.

Once again, it is useful to consider the specific internal energy distribution with radius at the final snapshot as seen in Fig 11. Comparisons with the initial interior profile of the target are easily done, concluding that the giant impacts result in higher internal energies than a settling

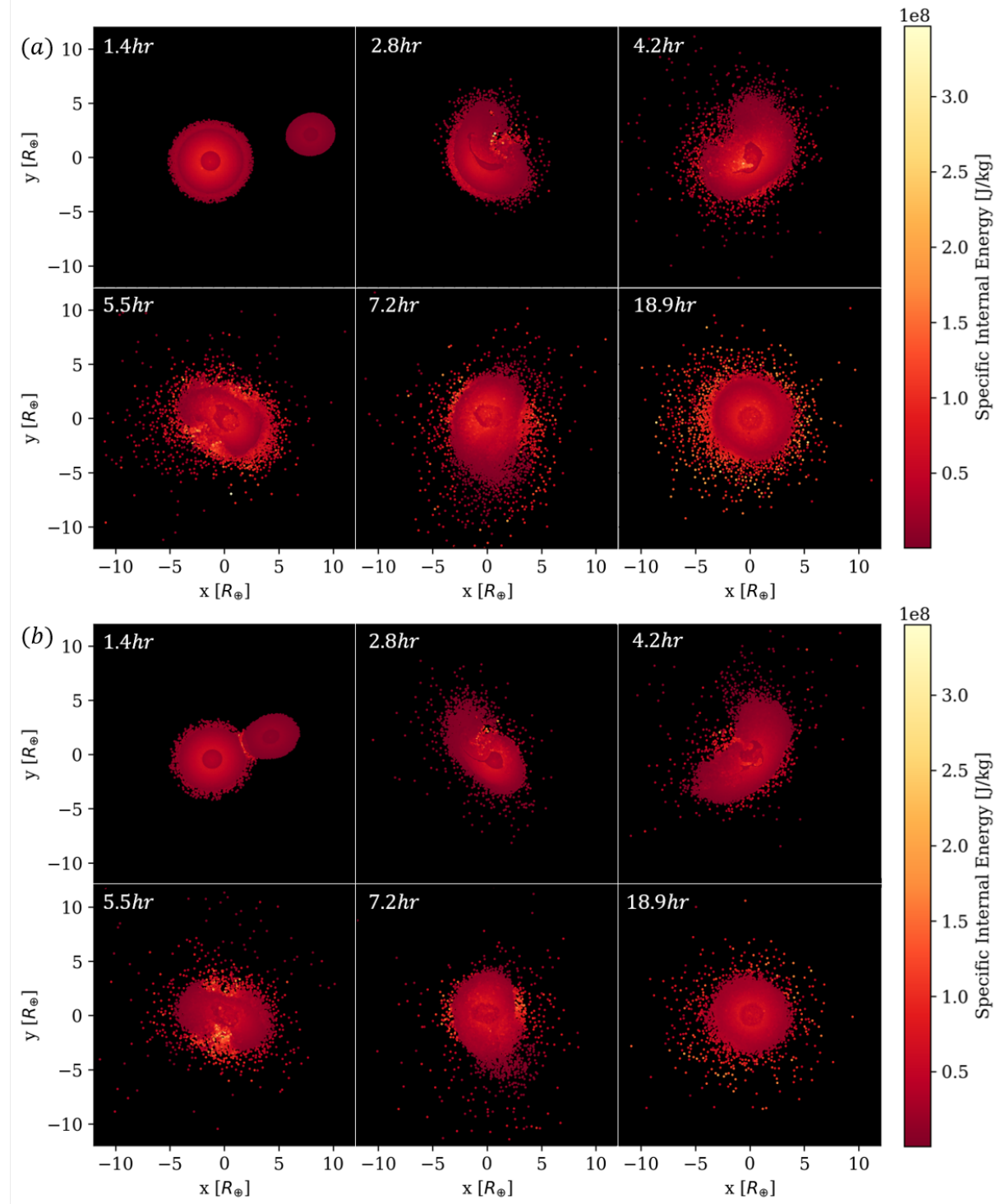


Figure 10: As in Fig 6, however, the colour gradient now shows the internal energy distribution. U-1 is shown in (a) and U-2 in (b). The 5.5hr and 7.2hr timesteps in each simulation reach the highest specific internal energy values of order 10^8 J/kg.

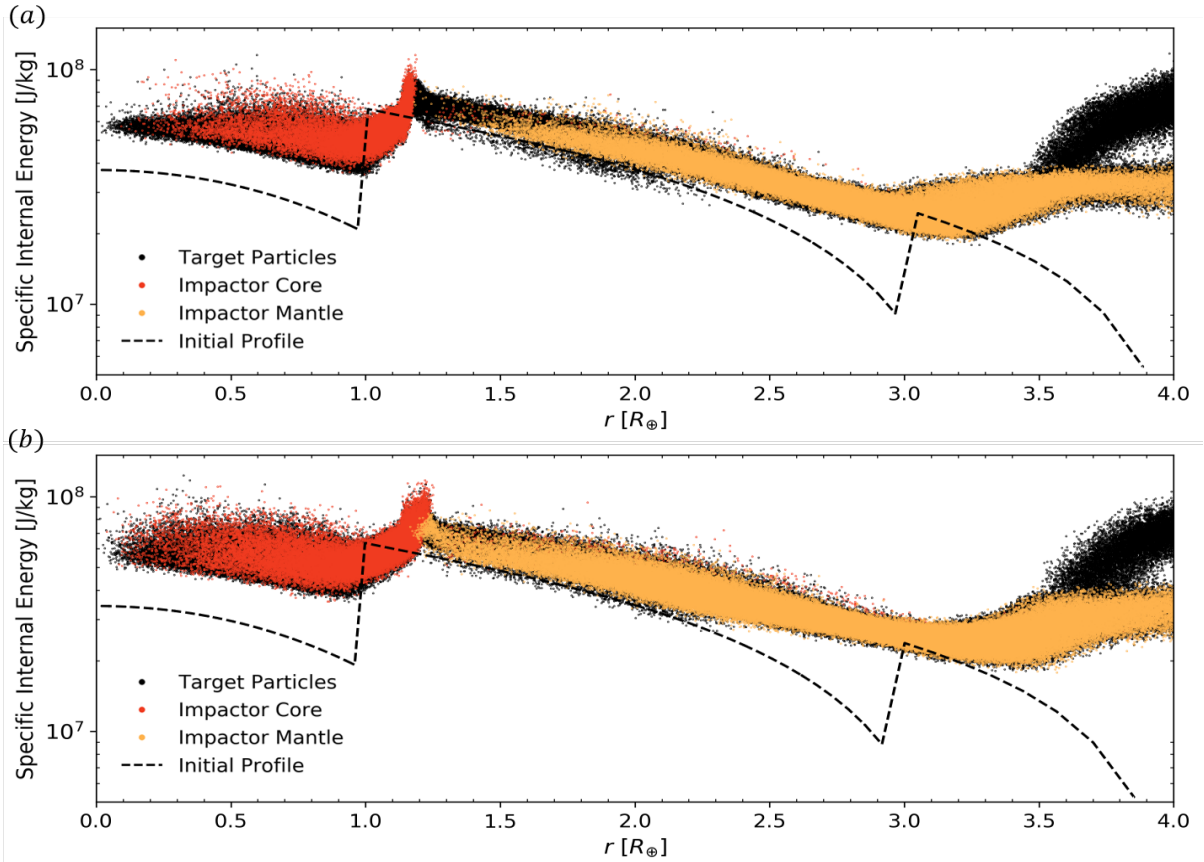


Figure 11: Specific internal energy distribution with radius of particles in the (a) U-1 and (b) U-2 simulation. The initial profile for the specific internal energy distribution for each pre-impact proto-Uranus is shown as a dotted line on each graph for reference. This is chosen given that the deviation of the planet after settling in Fig 4 had a small absolute deviation from this profile.

simulation without an impact. The peak at the core-mantle boundary for the proto-Uranus suggests a higher temperature gradient, ∇_T , than that of an adiabat, ∇_{ad} , suggesting that with a high molecular gradient, ∇_μ , at this boundary, overturning convection is unlikely while a system of layered convection within small cells tending towards a state of turbulent diffusion as in Fig 1 is much more probable. Given that this is determined from considering the internal energies and previously, in Section 3.1.2, it was demonstrated that large scale coverage of a sphere around the core-mantle boundary can be achieved through these impacts, this is significant towards understanding the contribution of giant impacts to the heat flux from the planet.

4 Discussion

Here, we discuss results from the above simulations and consider factors that could influence these, whilst also considering them in the wider scheme of alternative hypotheses to explain the comparatively low heat flux. We examine the EoS used, the albedo measurement determined from Voyager 2, and whether a divergence from this value is capable of explaining the current surface temperature. Furthermore, the potential of giant impacts to explain the diversity of exoplanets observed today are noted as well as potential progress using alternative numerical

models such as magnetohydrodynamics and general circulation models in future simulations.

4.1 Equations of State

Despite the fact that numerous authors have used and cited the HM80 EoS throughout their work, there has been concern raised by [Fortney et al. \(2011\)](#) for using them. They consider the H-He atmosphere equation of state to be the most questionable due to the fact that the behaviour of this mixture is difficult to study in Earth laboratories. Also, many of the EoS used for the layers in HM80 have since been updated following better understanding in how these materials behave.

At present, the HM80, Sesame and Tillotson EoS are the most frequently used to model planetary interiors, although [Vazan & Helled \(2019\)](#) use their own version for the proto-Uranus based on the quotidian equation of state from [More et al. \(1988\)](#). For the proto-Uranus, [Fortney et al. \(2011\)](#) show that as a replacement to the HM80 EoS, one could use the [Saumon et al. \(1995\)](#) EoS for the H-He atmosphere, Sesame "water 7154" for the icy-mantle and the Sesame "dry sand" ([Lyon & Johnson, 1992](#)) for the rocky core. Using their atmospheric cooling model, this reproduces the result that the present day Uranus is far less luminous than predicted. Work is therefore needed to determine which EoS are the most reliable for each region of the planet and to use these in future investigations.

Moving beyond the EoS, [Fortney et al. \(2011\)](#) also suggest that further updates to include the opacity of clouds and hazes are necessary as there is currently no theory capable to explain how various factors such as solar luminosity, effective temperature, and mixing on the planet may affect the opacity of these and their influence on the albedo. Opacity sources are an important consideration in any cooling model as they are key to determining radiative properties of model atmospheres. The databases for these have been continually updated but only began to enter model atmospheres in the new millennium. Further work is also needed to fill in crucial gaps in these databases considering low temperature CH₄ and H₂ collision-induced absorption ([Fortney et al., 2011](#)), both of which would be fundamental when applying model atmospheres to the ice giants.

4.2 Bond Albedo Uncertainty

Despite many researchers running long term temperature evolution models assuming a bond albedo of $A = 0.300$ as calculated from the Voyager 2 data, $A = 0.300 \pm 0.049$ ([Pearl et al., 1990](#)), recent remarks from [Scheibe et al. \(2019\)](#) suggest that changing the bond albedo within these cooling models to $A = 0.400$ is sufficient to reproduce cooling times aligned with the solar system age. At only a difference of $\sim 2\sigma$ from the Voyager value, this might not be a significant departure. Additional models determining the cooling times whilst changing the bond albedo, prior to the Voyager flyby, were also conducted by HM80. At this time the bond albedo was only determined theoretically with an estimate of $A = 0.37 \pm 0.05$ ([Dlugach & Yanovitskij, 1974](#)). Varying this to $A = 0.48$, they quote the corresponding equilibrium temperature of the planet is reduced to 54K, only $\sim 3\text{K}$ different from the observed value of $58.2 \pm 1\text{K}$ when including uncertainties ([Pearl et al., 1990](#)).

The paper in question quote that the primary issues in the Voyager measurements are due to uncertainties in the phase integral, as in Section 2.1.1, and the thermal emission calculations, where this is extrapolated from infrared to spectral regions not covered by the Voyager infrared spectrometer and radiometer (IRIS) (Pearl et al., 1990). Issues with the phase integral were a result of the flight path of Voyager; whilst providing up-close images of the planet, ideal full-disc measurements over the complete range of phase angles necessary to calculate the phase integral in (1) was not possible due to its close proximity. As mentioned previously, the only phase angles covered by IRIS data were $15^\circ < \alpha < 155^\circ$. The combination of this close proximity and phase angle range results in incomplete coverage of the planet, requiring an alternative method to describe the photometric behaviour. A scaling relation was utilised to derive complete disc measurements, and due to ground-based observations showing seasonal variations in these values for the Northern and Southern hemispheres, as illustrated by the increase in geometric albedo of $14 \pm 5\%$ between equinox in 1961 – 1963 from Lockwood et al. (1983), a decrease in the bond albedo determined from Voyager measurements of $7 \pm 3\%$ was included for the annual mean bolometric measurement (Pearl et al., 1990).

Furthermore, a variation in bond albedo measurements of Jupiter from Voyager and more recent satellites has been shown previously. The Cassini flyby of Jupiter presented a value of $A = 0.503 \pm 0.012$ (Li et al., 2018), whereas Voyager determined the value to be $A = 0.343 \pm 0.032$ (Hanel et al., 1981). This difference of 5σ , using the error from Voyager, is much greater than the difference used by Scheibe et al. (2019) to explain Uranus' cooling time and therefore this appears to be a plausible mechanism to explain the current temperature. Further research may also be required to consider the nature to which the bond albedo might change throughout the planet's evolution and how this would impact the cooling rate.

One might also consider whether the New Horizons mission, launched in 2005 towards Pluto, would be able to provide data to calculate the bond albedo. Unfortunately, New Horizons was in hibernation mode during the flyby of Uranus so no images or data were taken. However, due to the large distances from the planet, at about a quarter of its orbit away from New Horizons, even if the spacecraft was active during this flyby, any observations made would have limited use.

Since there has not been a dedicated mission to the ice giants, a new mission now may present results that can explain the anomalies in the heat flux and magnetosphere as described previously. Updated measurements for the bond albedo will also be necessary to explore cooling models more thoroughly. Scientists are already advocating such an ice giants mission (Arridge et al., 2014) as this would provide additional data to test existing theories to. This would be useful for not only our solar system and it's formation, in line with ESA's Cosmic Vision theme 'How does the Solar System work?', but also planetary sciences beyond because mini-Neptunes, alongside super-Earths, make up the majority of confirmed exoplanets (Fulton et al., 2017).

4.3 Exoplanet Diversity

The diversity of the exoplanets observed may be accountable, in part, to giant impacts of this nature. A summary of how this is possible is best achieved by considering the wider solar system. For example, it is well known that the formation of our own Moon is hypothesised to be a consequence of a giant imapct event between a Mars-sized object and the Earth (Halliday,

2000; Canup & Asphaug, 2001). In addition to this, impacts can also explain characteristics of other planets in our solar system.

Firstly, the geology of Mars has been considered with the inclusion of a giant impact. This is the case as a disparity between the Northern and Southern hemisphere of the planet has been observed, known as the hemispheric dichotomy, where the southern region is $\sim 4\text{km}$ higher than the northern region. Kiefer (2008) consider that this can be explained by a giant impact with support from Andrews-Hanna et al. (2008). This giant impact may, in a similar nature to our Moon, form the two moons of Mars, Phobos and Diemos as Rosenblatt et al. (2016) showed using numerical simulations that these can form from the debris post-impact.

Giant impact events may also assist in explaining why some planets, for example WASP-121b, are observed to have a much higher observed metallicity closer to the surface than can be explained using standard models such as a solar nebula theory alone. WASP-121b is a hot Jupiter observed with heavy elements iron and magnesium at high altitudes $R_{\text{planet}}/R_{\text{star}} \sim 0.3$ (Sing et al., 2019). In this case Delrez et al. (2016) suggest that this is a consequence of the close proximity of the planet to the star, implying that there is potential that these extended heavy elements are due to tidal disruption. However, an impact could also dredge up these heavy elements from the core of a planet. An example of this in our own solar system is Jupiter, where the origin of heavy elements distributed up to half its radius has been questioned. As determined by Liu et al. (2019), this could be achieved by a head on collision into the planet, such that material formerly in the core could be dredged up further out to the surface, mixing with materials in outer layers. This state was then shown to be capable of remaining for times in line with the age of our solar system (Liu et al., 2019), further supporting the theory if this happened early in the solar system, during the late bombardment period.

The Nice and Grand Tack models provide additional support for these theories explaining the migration of giant planets, the properties of the terrestrial planets and the origin of the Late Heavy Bombardment period at ~ 3.9 Gyrs ago, bringing peak impact activity in the inner solar system (Tsiganis et al., 2005; Gomes et al., 2005; Walsh et al., 2011). Clement et al. (2018) go beyond this by showing using dynamical simulations that alterations to the Nice model can create large embryos which are either scattered outwards or inwards towards our terrestrials, potentially creating a reservoir of $0.25 - 2.5M_{\text{Mars}}$ embryos which are ejected or scattered and could provide the means for giant impacts.

The range of different planetary characteristics these impacts can create within our own solar system alone raises the questions as to how frequently these events occur and whether our solar system is unique hosting many events of this nature. More work is required to answer these and consider the consequences of these in exoplanetary systems.

4.4 Advancing Simulations

As computing systems advance, making more efficient use of nodes within supercomputers has been beneficial in accelerating the rate at which simulations are run and processed. This has allowed giant impact simulations at the highest resolution of 10^8 particles to be investigated (Kegerreis et al., 2019). As seen in Kegerreis et al. (2019), convergence tests using a range of particle numbers are used to check that results, such as the post-impact Uranus rotation rate,

converge as we increase the number of particles. They showed that $10^7 - 10^8$ particles appear sufficient to reproduce the results of major planetary characteristics, however, the particular quantity of interest will determine the extent of the resolution required, such that a higher still resolution might be necessary to resolve certain features such as the fluid dynamics on smaller scales. This lower bound of 10^7 throws doubt into the results here with just 10^6 , a consequence of time and data restraints, with the 10^6 simulations using the allocated 100GB space initially acquired on Hamilton alone. This will therefore need to be investigated at higher resolution in the future. In increasing the particle number further beyond 10^8 , the computation time will continue to increase and so utilising the highest resolution available now appears to be ample to produce compelling results.

Due to the varying timescales between simulations of a giant impact and its subsequent evolution, from the order of seconds to billions of years, it is currently not possible to connect these initial simulations to magnetohydrodynamic simulations (MHD) to determine whether this impact scenario correctly reproduces the magnetic field of Uranus to current observations. Nevertheless, [Tóth et al. \(2004\)](#) have been able to simulate the magnetosphere of Uranus during the Voyager 2 flyby, reproducing the measured field. This showed that the field was effectively stationary with respect to the corotating frame of the planet. As these simulations have yet to be run over timescales of the age of the solar system, or connecting them to a giant impact, thought to be a viable mechanism to create its peculiar characteristics, this will be something to work towards in the future. If these could be performed, then it would provide an opportunity to connect thermal and magnetosphere measurements from Voyager 2 to our models of these. A science mission to the ice giants would also provide valuable data to test these magnetosphere models further.

Additionally, it may be useful to consider general circulation models (GCM) to study the long term evolution of the atmosphere. An example of this is the open source THOR GCM, which has been developed for exoplanet models ([Deitrick et al., 2019](#)). Applying these for Uranus would be able to assist in understanding atmospheric behaviour and fluid structures in the planet, but similarly to MHD simulations, the issue of timescales becomes apparent here. Furthermore, [Irwin et al. \(2017\)](#) mentions that although these would be useful to examine how the atmosphere changes over seasons, these can't currently be used due to the limited number of measurements presently available for the temperature of the planet which are unable to sufficiently constrain these models. Again, this provides another incentive for a future mission to these ice giants.

5 Conclusion

An investigation into possible explanations of the low heat flux of Uranus has been conducted. These include: a period of accelerated cooling ([Kurosaki & Ikoma, 2017](#)), a variation to the currently accepted bond albedo for the planet from Voyager 2 from $A = 0.300 \pm 0.049$ ([Pearl et al., 1990](#)) to $A = 0.4$ ([Scheibe et al., 2019](#)), and finally the giant impact hypothesis.

As mentioned previously, the limit to considering a different bond albedo value is that spacecraft data is required to complete the calculation accurately. Although we cannot check this at present, it is worth keeping in mind and considering how these different ideas may be

combined. For example, a period of accelerated cooling could be created from a giant impact event sufficiently polluting the atmosphere and this may have occurred alongside a different bond albedo to our present value.

Alternative suggestions would be required to consider the evolution without the impact event in order to explain its obliquity. One of these is through migration and perturbations in the early solar system where as Uranus and Saturn move towards each other they acquire their relative obliquities ([Brunini, 2006](#)). Here, the larger obliquities of Uranus are more easily obtained when the initial position of Uranus is outside the orbit of Neptune and then moves inwards. Despite this being able to explain the obliquity, additional factors would need to be considered to explain the low heat flux.

Also, as suggested by [Morbidelli et al. \(2012\)](#), in order to explain the prograde motion of the regular satellites of Uranus, a deviation in the planet's obliquity prior to the primary giant impact may be required. As multiple giant impacts into a planet have not yet been investigated, this might prove interesting. For now, we reiterate that a primary impact alone does sufficiently describe many of the characteristics of Uranus and increasing to more than one impact would vastly increase the parameter space within which we can explore.

The giant impact hypothesis is currently the most capable of describing the characteristics of the planet such as its rotation rate and obliquity. We found that the peak coverage of the proto-Uranus around the core-mantle boundary from the impactor's core material can be as high as 65 – 72% once overlapping of particle areas is removed. Furthermore, higher internal energies of particles towards the outside of the planet may allow for greater heating rates during and shortly after the impact, along with potential for small cell layered convection and turbulent diffusion. Therefore, this adds to the potential of the giant impact hypothesis to be a plausible mechanism to inhibit heat transfer out of the core as suggested by [Podolak et al. \(1991\)](#). With more time, higher particle simulations are desirable to ensure that results are considered to be in the converged regime and the fluid structures can be thoroughly investigated. These simulations would ideally then be connected to cooling models to consider the long term evolution of the planet.

Acknowledgements

Many thanks go to Dr. Eke for his guidance and support with this project. Additional thanks go to Dr. Kegerreis for the many fruitful discussions and advice with running these simulations.

References

- Andrews-Hanna J. C., Zuber M. T., Banerdt W. B., 2008, [Nature](#), **453**, 1212
- Arridge C., et al., 2014, [Planetary and Space Science](#), **104**, 122
- Brunini A., 2006, [Nature](#), **440**, 1163
- Canup R. M., Asphaug E., 2001, [Nature](#), **412**, 708
- Chesley S. R., Chodas P. W., Milani A., Valsecchi G. B., Yeomans D. K., 2002, [Icarus](#), **159**, 423
- Clement M. S., Kaib N. A., Raymond S. N., Walsh K. J., 2018, [Icarus](#), **311**, 340

- Deitrick R., Mendonça J. M., Schroffenegger U., Grimm S. L., Tsai S.-M., Heng K., 2019, arXiv e-prints, p. [arXiv:1911.13158](https://arxiv.org/abs/1911.13158)
- Delrez L., et al., 2016, *MNRAS*, **458**, 4025
- Dlugach J. M., Yanovitskij E. G., 1974, *Icarus*, **22**, 66
- Fletcher L. N., et al., 2019, arXiv e-prints, p. [arXiv:1907.02963](https://arxiv.org/abs/1907.02963)
- Fortney J. J., Ikoma M., Nettelmann N., Guillot T., Marley M. S., 2011, *The Astrophysical Journal*, **729**, 32
- Fulton B. J., et al., 2017, *AJ*, **154**, 109
- Gall J., 1885, *Scottish Geographical Magazine*, **1**, 119
- Glatzmaier G. A., 2014, Introduction to Modeling Convection in Planets and Stars: Magnetic Field, Density Stratification, Rotation, stu - student edition edn. Princeton University Press, <http://www.jstor.org/stable/j.ctt4cgcb1>
- Gomes R., Levison H. F., Tsiganis K., Morbidelli A., 2005, *Nature*, **435**, 466
- Gómez-Pérez N., Heimpel M., 2007, *Geophysical and Astrophysical Fluid Dynamics*, **101**, 371
- Halliday A. N., 2000, *Earth and Planetary Science Letters*, **176**, 17
- Hanel R., Conrath B., Herath L., Kunde V., Pirraglia J., 1981, *Journal of Geophysical Research*, **86**, 8705
- Hanel R. A., Conrath B. J., Kunde V. G., Pearl J. C., Pirraglia J. A., 1983, *Icarus*, **53**, 262
- Hanel R., et al., 1986, *Science*, **233**, 70
- Hubbard W. B., 1973, *Space Science Reviews*, **14**, 424
- Hubbard W. B., 1977, *Icarus*, **30**, 305
- Hubbard W. B., 1978, *Icarus*, **35**, 177
- Hubbard W. B., Macfarlane J. J., 1980, *Journal of Geophysical Research*, **85**, 225
- Irwin P., Tice D., Fletcher L., Barstow J., Teanby N., Orton G., Davis G., 2015, *Icarus*, **250**, 462
- Irwin P. G. J., Fletcher L. N., Read P. L., Tice D., de Pater I., Orton G. S., Teanby N. A., Davis G. R., 2016, *Icarus*, **264**, 72
- Irwin P. G., Wong M. H., Simon A. A., Orton G., Toledo D., 2017, *Icarus*, **288**, 99
- Ishizawa Y., Sasaki T., Hosono N., 2019, *ApJ*, **885**, 132
- Kegerreis J. A., et al., 2018, *ApJ*, **861**, 52
- Kegerreis J. A., Eke V. R., Gonnet P., Korycansky D. G., Massey R. J., Schaller M., Teodoro L. F. A., 2019, *MNRAS*, **487**, 5029
- Kiefer W. S., 2008, *Nature*, **453**, 1191
- Kurosaki K., Ikoma M., 2017, *The Astronomical Journal*, **153**, 260
- Kurosaki K., Inutsuka S.-i., 2018, *The Astronomical Journal*, **157**, 13
- Leconte J., Chabrier G., 2012, *A&A*, **540**, A20
- Ledoux P., 1947, *The Astronomical Journal*, **52**, 155
- Li L., et al., 2018, *Nature Communications*, **9**, 3709
- Lindal G. F., Lyons J. R., Sweetnam D. N., Eshleman V. R., Hinson D. P., Tyler G. L., 1987, *Journal of Geophysical Research*, **92**, 14987
- Liu S.-F., Hori Y., Müller S., Zheng X., Helled R., Lin D., Isella A., 2019, *Nature*, **572**, 355
- Lockwood G. W., Lutz B. L., Thompson D. T., Warnock A., 1983, *ApJ*, **266**, 402
- Lyon S. P., Johnson J. D., 1992, SESAME: THE LOS ALAMOS NATIONAL LABORATORY EQUATION OF STATE DATABASE

- Monaghan J. J., 1992, *Annual Review of Astronomy and Astrophysics*, **30**, 543
- Morbidelli A., Tsiganis K., Batygin K., Crida A., Gomes R., 2012, *Icarus*, **219**, 737
- More R. M., Warren K. H., Young D. A., Zimmerman G. B., 1988, *Physics of Fluids*, **31**, 3059
- Nellis W. J., 2015, arXiv e-prints, p. [arXiv:1503.01042](#)
- Nettelmann N., Helled R., Fortney J. J., Redmer R., 2013, *Planet. Space Sci.*, **77**, 143
- Pearl J. C., Conrath B. J., 1991, in . p. 1154
- Pearl J., Conrath B., Hanel R., Pirraglia J., Coustenis A., 1990, *Icarus*, **84**, 12
- Podolak M., Hubbard W. B., Stevenson D. J., 1991, Models of Uranus' interior and magnetic field.. pp 29–61
- Podolak M., Weizman A., Marley M., 1995, *Planetary and Space Science*, **43**, 1517
- Price D. J., 2008, *Journal of Computational Physics*, **227**, 10040
- Price D. J., 2012, *Journal of Computational Physics*, **231**, 759
- Reinhardt C., Chau A., Stadel J., Helled R., 2019, *MNRAS*, p. [2855](#)
- Rosenblatt P., Charnoz S., Dunseath K. M., Terao-Dunseath M., Trinh A., Hyodo R., Genda H., Toupin S., 2016, *Nature Geoscience*, **9**, 581
- Safronov V. S., 1966, Sov. Astron, **9**, 987
- Saumon D., Chabrier G., van Horn H. M., 1995, *The Astrophysical Journal Supplement Series*, **99**, 713
- Scheibe L., Nettelmann N., Redmer R., 2019, arXiv e-prints, p. [arXiv:1911.00447](#)
- Schwarzschild K., 1906, Nachrichten von der Königlichen Gesellschaft der Wissenschaften zu Göttingen. Math.-phys. Klasse, **195**, 41
- Sing D. K., et al., 2019, *The Astronomical Journal*, **158**, 91
- Slattery W. L., Benz W., Cameron A., 1992, *Icarus*, **99**, 167
- Stanley S., Bloxham J., 2004, in AGU Spring Meeting Abstracts. pp GP33A–01
- Stevenson D. J., 1986, in Lunar and Planetary Science Conference. Lunar and Planetary Science Conference. pp 1011–1012
- Tóth G., Kovács D., Hansen K. C., Gombosi T. I., 2004, *Journal of Geophysical Research (Space Physics)*, **109**, A11210
- Tremaine S., 1991, *Icarus*, **89**, 85
- Tsiganis K., Gomes R., Morbidelli A., Levison H. F., 2005, *Nature*, **435**, 459
- Vazan A., Helled R., 2019, arXiv e-prints, p. [arXiv:1908.10682](#)
- Vazan A., Helled R., Kovetz A., Podolak M., 2015, *The Astrophysical Journal*, **803**, 32
- Walsh K. J., Morbidelli A., Raymond S. N., O'Brien D. P., Mandell A. M., 2011, *Nature*, **475**, 206
- Warwick J. W., et al., 1986, *Science*, **233**, 102
- Zharkov V. N., Trubitsyn V. P., 1978, Physics of planetary interiors
- de Pater I., Lissauer J. J., Hubbard W. B., 2002, *Physics Today*, **55**, 64
- de Pater I., Sromovsky L., Fry P., Hammel H. B., Baranec C., Sayanagi K. M., 2015, *Icarus*, **252**, 121